*J. Fluid Mech.* (1995), *vol.* 287, *pp.* 173–197



# A mathematical analysis of the steady response of floating ice to the uniform motion of a rectangular load

By F. MILINAZZO[1], MARVIN SHINBROT[2]† AND N. W. EVANS[2]

[1] Mathematics Department, Royal Roads Military College, FMO Victoria, B.C., Canada V0S 1B0

[2] Mathematics Department, University of Victoria, Victoria, B.C., Canada V8W 2Y2

(Received 15 June 1994 and in revised form 26 October 1994)

In this article, we considered the steady response of an infinite unbroken floating ice sheet to the uniform motion of a rectangular load. It is assumed that the ice sheet is supported below by water of finite uniform depth. The ice displacement is expressed as a Fourier integral and the method of residues is combined with a numerical quadrature scheme to calculate the displacement of the surface. In addition, asymptotic estimates of the displacement are given for the far field and for the case where the aspect ratio of the load is large. The far-field approximation provides a good description of the surface displacement at distances greater than about one or two wavelengths away from the load. The behaviour of the steady solution at the two critical speeds $U_m$, where the phase speed takes on its minimum, and $U_g$, the speed of gravity waves on shallow water, observed in Schulkes & Sneyd (1988) for an impulsively started line load is examined to see if these speeds are critical for two-dimensional loads. Unlike the steady part of the solution in Schulkes & Sneyd (1988), the solution is everywhere finite at the critical speed $U_g$. However, at the load speed $U_m$, the solution is unbounded. At all load speeds the change in surface displacement is greatest near the load. A comparison with the experimental observations of Takizawa (1985) is made. Our calculations show a significant dependence of the amplitude of the ice displacement on the aspect ratio of the load. For wide loads the surface deflection has much more structure than does the surface displacement corresponding to loads of smaller aspect ratios.

## 1. Introduction

Some time ago it was observed that air cushion vehicles could be used to rupture ice by taking advantage of the fact that moving loads can generate waves in both ice and water (see Eyre 1977; Brochu 1977). Under certain conditions the disturbance is of sufficient amplitude to break the ice. Since in many areas winter ice cover forms an integral part of the transportation system by transforming bodies of water into roads and runways, it is important to determine the load levels that can be safely supported. In other areas the focus is on breaking the ice in order to facilitate water traffic. An effective method of ice breaking not only increases the period of time during which waterways can be navigated, but also provides a means of flood control.

One of the first theoretical studies of the response of floating ice to moving loads was given in Greenhill (1887). More recently, a number of authors: Kheisin (1963, 1971),

† Deceased.

Nevel (1970), Kerr (1983), Davys, Hosking & Sneyd (1985), Schulkes, Hosking & Sneyd (1987), and Schulkes & Sneyd (1988) have studied the effects of a moving load on floating ice. In these investigations, the ice sheet is treated as a thin plate of infinite extent supported below by water of uniform, finite depth and the load is assumed to move with constant speed. Kheisin (1963) examines the steady motion of a point and a line load. For a point load, he wrongly concludes that the deflection is bounded for all source speeds, while for a line load, he finds two critical speeds at which the ice deflection is unbounded. Nevel (1970) considers the steady motion of a load uniformly distributed over a disk and concludes that there exists a single critical speed at which the deflection is infinite. Although Nevel examines the dependence of this critical speed on problem data, his main concern is with the ice displacement and stresses at the centre of the load as a function of source speed. Experimentally, a dependence of wave amplitude on load speed has been observed and measured (see for example Beltaos 1980; Cohen & Clayton 1982; Takizawa 1985, 1988). Davys *et al.* (1985) give a description of the far-field wave pattern caused by the steady motion of a point source. In addition, they compare their results to field measurements of the displacement and stresses at a point far from the load. In an attempt to explain the existence of critical speeds, Kheisin (1971) and Schulkes & Sneyd (1988) study the effect of an impulsively started, steadily moving line load. In particular, Schulkes & Sneyd (1988) show that there are two critical speeds, $U_m$ and $U_g$, for which the solution grows with time. The speed $U_m$ is the minimum of the dispersion relation given in Greenhill (1887) and corresponds to the critical speed identified by Nevel (1970). In addition, they note that wavecrests produced by a two-dimensional load moving with speed $U_m$ would be parallel to one another and perpendicular to the direction of motion. Consequently, energy can propagate only in the direction of motion. Hence, it is expected that $U_m$ will remain a critical speed for two-dimensional sources. Moreover, Davys *et al.* (1985) point out that at this load speed, the minimum phase speed coincides with the group speed. Consequently, in the absence of dissipation, energy must accumulate beneath a uniformly moving load. The other critical speed $U_g = (gH)^{1/2}$ corresponds to the speed of gravity waves propagating on shallow water of uniform depth. Here, Schulkes & Sneyd (1988) observe that energy can radiate away from the direction of travel and it is possible that $U_g$ is not a critical speed for two-dimensional sources. It is worth noting that the steady part of the solution given by Schulkes & Sneyd (1988) becomes unbounded as the load speed approaches these values.

Much of our work was motivated by the interest of Transport Canada in the use of air cushion vehicles for breaking ice. Their experience shows that when ice rupture occurs, it does so behind and near the vehicle. Consequently, we are interested in the solution in the vicinity of the load where asymptotic estimates are not available. In what follows, we re-derive Nevel's solution but for a uniform, rectangular pressure distribution of length $2b$ and width $2a$. The load is oriented so that the width is in the direction of travel. In using the Fourier transform to determine the steady waveform, we note that it is necessary to introduce time dependence in order to ensure that the solution obtained satisfies the correct radiation condition. Our numerical approximation to the solution gives an accurate and detailed description of the ice deflection over the entire flow field for all load speeds not equal to $U_m$. The result corresponds to the steady part of the solution of Schulkes & Sneyd (1988) for a two-dimensional load. A simple analysis of the poles of the integrand of the Fourier integral shows that no steady solution is possible when the load speed is $U_m$. On the other hand, when the speed of the load is $U_g$, we see that the displacement of the waveform is finite. Hence, our calculations support the claim of Davys *et al.* (1985) and Schulkes & Sneyd (1988)

that $U_m$ remains a critical speed for two-dimensional sources. However, we conclude that $U_g$ is not a critical speed for two-dimensional loads in the sense that the steady deflection of the ice sheet is bounded at this load speed. The infinite deflection of the steady part of the solution of Schulkes & Sneyd (1988) is an artifact of the dimensionality of the source. Whether the solution of the initial value problem for a two-dimensional load moving with this speed grows with time remains an open question. In view of the work of Schulkes & Sneyd (1988), it is clear that for a given load speed there is a dependence of the deflection of the ice on the aspect ratio of the pressure distribution. We investigate this relationship and find a significant dependence, particularly for load speeds between $U_m$ and $U_g$. An asymptotic estimate of the ice deflection for large $b$ is given.

The paper is organized as follows. In §2 the problem is formulated as a Fourier integral. The details of the analysis of the singularities of the integrand are given in Appendix A. The results of an asymptotic analysis of the solution are given in §3. The details are left to Appendix B. In §4 a numerical method for approximating the solution is detailed. Finally, in §5 some numerical results are presented and a comparison with the experimental results of Takizawa (1985) is made.

## 2. Formulation of the problem

In formulating the problem, we take the $(x, z)$-plane to coincide with the ice sheet, the gravitational acceleration $g$ is taken to be in the negative $y$-direction, and time is denoted by $t$. We assume an infinite, unbroken ice field that can be treated as a thin plate of constant thickness $h$ and density $\rho'$. Moreover, the water body is taken to be of constant density $\rho$ and uniform depth $H$. We assume that the fluid motion beneath the ice is irrotational and incompressible and can be described by a velocity potential $\phi$. In a frame of reference moving with the load speed $U$, in the negative $x$-direction, the equation of motion (see Szilard 1974) for the vertical deflection $\eta$ of a thin plate supported below by water and supporting a pressure distribution $P$ is

$$D\left(\frac{\partial^2}{\partial x^2}+\frac{\partial^2}{\partial z^2}\right)^2\eta-p+\rho' h\left(\frac{\partial}{\partial t}+U\frac{\partial}{\partial x}\right)^2\eta=-P(x,z), \quad -\infty<x,z<\infty. \tag{2.1}$$

For a uniform plate, the constant $D$ is given in terms of Young's modulus $E$ and Poisson's ratio for ice $\sigma$ by the expression $D = Eh^3/[12(1-\sigma^2)]$. The water pressure $p(t, x, z)$ is determined from the equations (see Whitham 1974)

$$\phi_{xx}+\phi_{yy}+\phi_{zz}=0 \quad \text{for} \quad -H<y<0, \tag{2.2}$$

with

$$\phi_y(t,x,-H,z)=0, \quad \phi_y(t,x,0,z)=\left(\frac{\partial}{\partial t}+U\frac{\partial}{\partial x}\right)\eta, \tag{2.3}$$

and

$$g\eta+\frac{1}{\rho}p+\left(\frac{\partial}{\partial t}+U\frac{\partial}{\partial x}\right)\phi(t,x,0,z)=0. \tag{2.4}$$

The conditions given by (2.3) express the no-normal-flow condition at the bottom and the kinematic condition at the ice–water interface. The latter ensures that the vertical speed of the water at $y = 0$ and that of the ice sheet are the same. The Bernoulli condition (2.4) is a statement of force balance at the water–ice interface. Note that in using (2.4), we limit the discussion to linear disturbances.

In employing the Fourier transform to find the steady-state solution of (2.1)–(2.4), it is necessary to apply the correct radiation condition at infinity. To accomplish this, we resort to an artifice due to Lighthill (1957), see also Whitham (1974), and introduce an artificial time dependence. In (2.1), $P$ is replaced by $P^\delta = e^{\delta t} P$ where $\delta > 0$. This corresponds to a pressure source which was zero in the distant past and has grown to $P$ at $t = 0$. The steady-state solution of (2.1)–(2.4) is obtained by finding a solution of (2.1)–(2.4) with $P(x, z) = P^\delta$ and then letting $\delta \to 0$.

It is easy to see that the time dependence of the solution must be $e^{\delta t}$, that is $\eta(t, x, z) = e^{\delta t}\hat{\eta}^\delta(x, z)$, $\phi(t, x, y, z) = e^{\delta t}\hat{\phi}^\delta(x, y, z)$, and $p(t, x, z) = e^{\delta t}\hat{p}^\delta(x, z)$. In this notation, the steady-state solution of (2.1)–(2.4) is $\hat{\eta}^0$, $\hat{\phi}^0$, $\hat{p}^0$. Making these substitutions into (2.1)–(2.4), taking the Fourier transform in both the $x$- and $z$-directions and using the definition

$$\mathscr{H}^\delta(\kappa_1, \kappa_2) = \frac{1}{2\pi}\int_{-\infty}^{\infty}\int_{-\infty}^{\infty}\hat{\eta}^\delta e^{i(x\kappa_1 + z\kappa_2)}\,dx\,dz,$$

together with corresponding definitions for $\Phi^\delta$, $\mathscr{P}^\delta$, and $\Pi$, the transforms of $\hat{\phi}^\delta, \hat{p}^\delta$, and $P$ respectively, gives

$$(D\kappa^4 + \rho' h(\delta - iU\kappa_1)^2)\mathscr{H}^\delta - \mathscr{P}^\delta = -\Pi, \tag{2.5}$$

$$\Phi^\delta_{yy} - \kappa^2\Phi^\delta = 0 \quad \text{for} \quad -H < y < 0, \tag{2.6}$$

$$\Phi^\delta_y(\kappa_1, \kappa_2, -H) = 0, \quad \Phi^\delta_y(\kappa_1, \kappa_2, 0) = (\delta - iU\kappa_1)\mathscr{H}^\delta, \tag{2.7}$$

$$g\mathscr{H}^\delta + \frac{1}{\rho}\mathscr{P}^\delta + (\delta - iU\kappa_1)\Phi^\delta(\kappa_1, \kappa_2, 0) = 0, \tag{2.8}$$

where $\kappa^2 = \kappa_1^2 + \kappa_2^2$.

Using (2.5)–(2.8), introducing the parameters $\mu = \rho'/\rho, \gamma = \mu h/H, \alpha = D/(\rho g H^4) = Eh^3/(12\rho g(1-\sigma^2)H^4)$, $F^2 = U^2/gH$, $k = H\kappa$, $k_1 = H\kappa_1, k_2 = H\kappa_2$ and redefining $\delta H/U$ as $\delta$, it is easy to see that, in a frame of reference moving with the load, the steady-state displacement is given by

$$\hat{\eta}^o(x, z) = \frac{1}{2\pi\rho g H^2}\lim_{\delta\to 0}\int_{-\infty}^{\infty}\int_{-\infty}^{\infty}\frac{\Pi k\tanh k\, e^{-i((x/H)k_1 + (z/H)k_2)}}{F^2(k_1 + i\delta)^2(1 + \gamma k\tanh k) - k\tanh k(1 + \alpha k^4)}\,dk_1\,dk_2. \tag{2.9}$$

Similar expressions can be obtained for $\hat{\phi}^o$ and $\hat{p}^o$.

The load is

$$P(x, z) = \begin{cases} P_o & x \in [-a, a], z \in [-b, b], \\ 0 & \text{otherwise}, \end{cases} \tag{2.10a}$$

with Fourier transform

$$\Pi = \frac{2P_o H^2}{\pi}\frac{\sin[ak_1/H]}{k_1}\frac{\sin[bk_2/H]}{k_2}. \tag{2.10b}$$

Substituting $\Pi$ from (2.10) into (2.9), we obtain

$$\hat{\eta}^o(x, z) = \frac{P_o}{\pi^2\rho g}\lim_{\delta\to 0}\int_{-\infty}^{\infty}\int_{-\infty}^{\infty}\frac{Q(k)}{\mathscr{D}^\delta(k_1, k_2)}e^{-i((x/H)k_1 + (z/H)k_2)}\frac{\sin[ak_1/H]}{k_1}\frac{\sin[bk_2/H]}{k_2}\,dk_1\,dk_2. \tag{2.11}$$

For convenience, we have introduced the functions

$$Q(k) = \frac{\tanh k}{k}\frac{1}{[1 + \gamma k\tanh k]}$$

and
$$\mathscr{D}^{\delta}(k_1, k_2) = F^2 \frac{(k_1 + \mathrm{i}\delta)^2}{k^2} - \frac{c^2}{gH}. \tag{2.12}$$

Here, $c$ is the phase speed of free waves. It can be derived from (2.1)–(2.4) by setting $P = 0$ and searching for solutions of the form $\mathrm{e}^{\mathrm{i}(\omega t - \kappa_1 x - \kappa_2 z)}$. The result is

$$c^2 = \left[\frac{\omega}{\kappa}\right]^2 = gH \frac{\tanh k}{k} \frac{1 + \alpha k^4}{1 + \gamma k \tanh k}. \tag{2.13}$$

To evaluate (2.11), we treat it as an iterated integral in $k_1$ and $k_2$. The $k_1$-integral is evaluated using the method of residues. The resulting $k_2$-integral can be approximated either numerically or asymptotically in the limit of large $|x|$ or large $b$.

At this point it should be stressed that $\delta$ serves only to determine how the above artificial time dependence moves the real poles into the complex $k_1$-plane, thus establishing whether the contour of integration is to be deformed into the upper or lower half-plane†. Consequently, we can set $\delta = 0$ and identify the poles as the roots in the complex $k_1$-plane of the equation

$$\mathscr{D}(k_1, k_2) \equiv \mathscr{D}^0(k_1, k_2) = 0, \tag{2.14}$$

for fixed $F^2$ and $k_2^2$.

There are two sets of poles. The first set contains an infinite number of points which lie on the imaginary axis for all values of $k_2$. These points can be determined by letting $k = \mathrm{i}\lambda$ in (2.14) and re-arranging to obtain

$$F^2\left(1 + \frac{k_2^2}{\lambda^2}\right) = \frac{\tan\lambda}{\lambda} \frac{(1 + \alpha\lambda^4)}{(1 - \gamma\lambda\tan\lambda)} = \frac{1}{\lambda} \frac{(1 + \alpha\lambda^4)}{(\cot\lambda - \gamma\lambda)}. \tag{2.15}$$

It is clear that the right-hand side of (2.15) is infinite at the points where $\cot\lambda = \gamma\lambda$. We label these points $\{\hat{\lambda}_j\}_{j=1}^{\infty}$. Since on the intervals $[j\pi, \hat{\lambda}_{j+1}]$, $(\tan\lambda/\lambda)(1 + \alpha\lambda^4)/(1 - \gamma\lambda\tan\lambda)$ is a monotone increasing function of $\lambda$, it is easy to see that there is an infinite set of points $\{\lambda_j\}_{j=1}^{\infty}$ where (2.15) is satisfied (see figure 1). It is clear that $\lambda_j \neq 0, j \geqslant 2$ for all values of $F^2$ and $k_2^2$. However, it is important to note that for $F^2 > 1$, $\lambda_1 \neq 0$ for all real values of $k_2^2$, while for $F^2 \leqslant 1$, $\lambda_1 \to 0$ as $k_2 \to 0$. In the $k_1$-plane, the poles are located at the points $\pm\mathrm{i}(\lambda_j^2 + k_2^2)^{1/2}$, $1 \leqslant j \leqslant \infty$.

The second set contains four points, one in each quadrant. Depending on the value of $F$, these four points can be real for a range of values of $k_2^2$. They are also symmetric about the imaginary axis, thus we need only consider the two points with non-negative real part. The dependence of these points on $F^2$ and $k_2^2$ can be seen by considering the intersection of the two curves

$$\frac{\tanh k}{k} \frac{1 + \alpha k^4}{1 + \gamma k \tanh k} = F^2 \frac{k_1^2}{k^2} = F^2\left(1 - \frac{k_2^2}{k^2}\right) \tag{2.16}$$

(see figure 2). This condition, given by Davys *et al.* (1985), states that for a steady wave pattern, the component of the source velocity normal to any wavecrest must be equal to the phase speed of the crest, that is

$$U^2 \cos^2\beta = c^2.$$

Here, $\beta$ is the angle between the load velocity and the wavenumber vector and $\cos\beta = k_1/k$.

† In many applications dissipation can be used to achieve the same purpose.

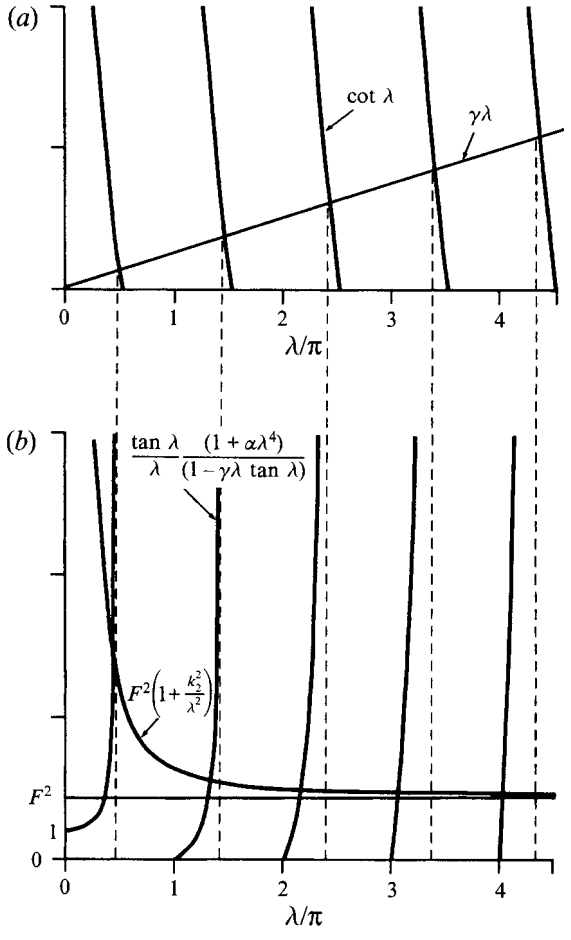


FIGURE 1. A schematic showing the position of the imaginary roots of $\mathscr{D}(k_1, k_2) = 0$ for fixed values of $k_2$: (*a*) the points of intersection of the curves $\cot\lambda$ and $\gamma\lambda$; (*b*) the points of intersection of the curves $[\tan\lambda(1+\alpha\lambda^4)]/[\lambda(1-\gamma\lambda\tan\lambda)]$ and $F^2(1+k_2^2/\lambda^2)$.

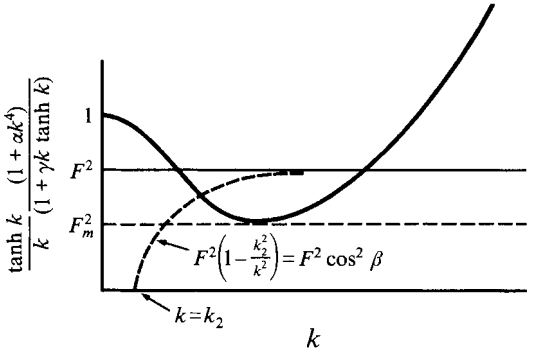


FIGURE 2. The dispersion relation $c^2/gH = [\tanh k/k][1+\alpha k^4]/[1+\gamma k\tanh k]$. The intersection of the dashed curve with the dispersion curve shows the position of the real roots of $\mathscr{D}(k_1, k_2) = 0$ for fixed $k_2$.

The right-hand side of (2.16) is the dispersion curve given by (2.13). Denoting the minimum of the left-hand side of (2.16) by $F_m^2$, we can see that the nature of the two poles will differ for each of the cases: (*a*) $F < F_m$, (*b*) $F = F_m$, (*c*) $F_m < F < 1$, (*d*) $F = 1$ or (*e*) $F > 1$. Figure 3(*a*) illustrates the five different cases. Davys *et al.* (1985) use (2.16) and the wavenumber curve to infer the emergence of a 'shadow zone' for $F^2 > 1$. The same conclusion can be drawn from figure 3(*a*)(v). For the corresponding values of $F$, figure 3(*b*) shows the paths followed by each of the four real poles as $k_2$ varies from zero to infinity. Also shown in figure 3(*b*) are the paths followed by the two poles $\pm i(\lambda_1^2+k_2^2)^{1/2}$ as functions of $k_2$. Here, it is important to notice that for $F^2 < 1$, these two imaginary poles coalesce as $k_2 \to 0$, while for $F^2 > 1$, $(\lambda_1^2+k_2^2)^{1/2} > 0$ for all $k_2$.

Here, we describe the nature of the poles in the second set as functions of $k_2^2$, and $F^2$. In Appendix A we give arguments to support our claims. For $F^2 < F_m^2$, the poles are complex with non-zero imaginary part for all real values of $k_2^2$. For $F^2 = F_m^2$ the poles are real when $k_2^2 = 0$, but have non-zero imaginary part for all $k_2^2 \neq 0$. The double root at $k_2^2 = 0$ leads to a singularity of the form $1/|k_2|$ in the $k_2$-integral. Since this singularity is not integrable, the ice deflection is unbounded. The corresponding load speed is $U_m$. In the case $F_m^2 < F^2 < 1$, the poles are real for $k_2 = 0$. As $k_2^2$ increases the poles approach one another, coalesce and separate into a complex conjugate pair. At the value of $k_2$ where the complex conjugate pair coalesce and the double real pole appears, the $k_2$ integral has a square root singularity. Clearly this value of $k_2$ depends on $F$. When $F^2 = 1$ and $k_2^2 \to 0$ the real poles of smaller magnitude and the two poles $\pm i(\lambda_1^2+k_2^2)^{1/2}$ approach the origin. The residue from these poles is proportional to $1/|k_2|^{1/2}$, and hence, the contribution from the poles to the $k_2$-integral is finite. The corresponding load speed is $U_g$. We conclude that $U_m$ is a critical speed for two-dimensional distributed loads. At the speed $U_g$ the ice displacement is bounded.

As indicated above, the role of $\delta$ is to determine whether the contour of integration is deformed into the upper or lower half plane. By expanding $\mathscr{D}^\delta(k_1, k_2)$ about a real root for small $\delta$, the sign of the imaginary part of the perturbation can be determined. The poles closest to the origin move into the lower half-plane, while those farthest from the origin move into the upper half-plane. As a consequence, we will see that the short capillary waves appear ahead of the load while the long gravity waves appear behind the load. These poles are denoted by $A$, $B$, $-\bar{A}$, and $-\bar{B}$. The poles in the upper half-plane are labelled $A$, while those in the lower half-plane are labelled $B$. The points $A$ and $B$ are taken to be in the right-hand plane. The above two sets of points comprise all poles of the integrand of (2.11) for all values of the parameters $F$, $\alpha$ and $\gamma$ (see Hosking, Sneyd & Waugh 1988).

Having identified the poles, it is straightforward to evaluate the $k_1$-integral by the method of residues. We first write (2.11) as

$$\hat{\eta}^o(x,z) = \frac{P_o}{\pi^2 \rho g} \lim_{\delta \to 0} \int_{-\infty}^{\infty} \frac{e^{-i((z/H)k_2)} \sin[bk_2/H]}{k_2} [G_-^\delta(k_2) - G_+^\delta(k_2)]\, dk_2, \tag{2.17}$$

where

$$G_\pm^\delta(k_2) = \frac{1}{2i} \int_{-\infty}^{\infty} \frac{Q(k)}{\mathscr{D}^\delta(k_1, k_2)} \frac{e^{-i(x/H \pm a/H)k_1}}{k_1} dk_1. \tag{2.18}$$

The evaluation of the integrals in (2.18) separates into three cases depending on whether $x$ is behind, within or in front of the load. Behind the load $x > a$, hence $x \pm a > 0$ and the integrals are evaluated by closing both contours in the lower half-plane. Within the load $-a < x < a$, hence $x+a > 0$ and $x-a < 0$ and consequently the contour for $G_+^\delta(k_2)$ must be closed in the lower half-plane, while the contour for

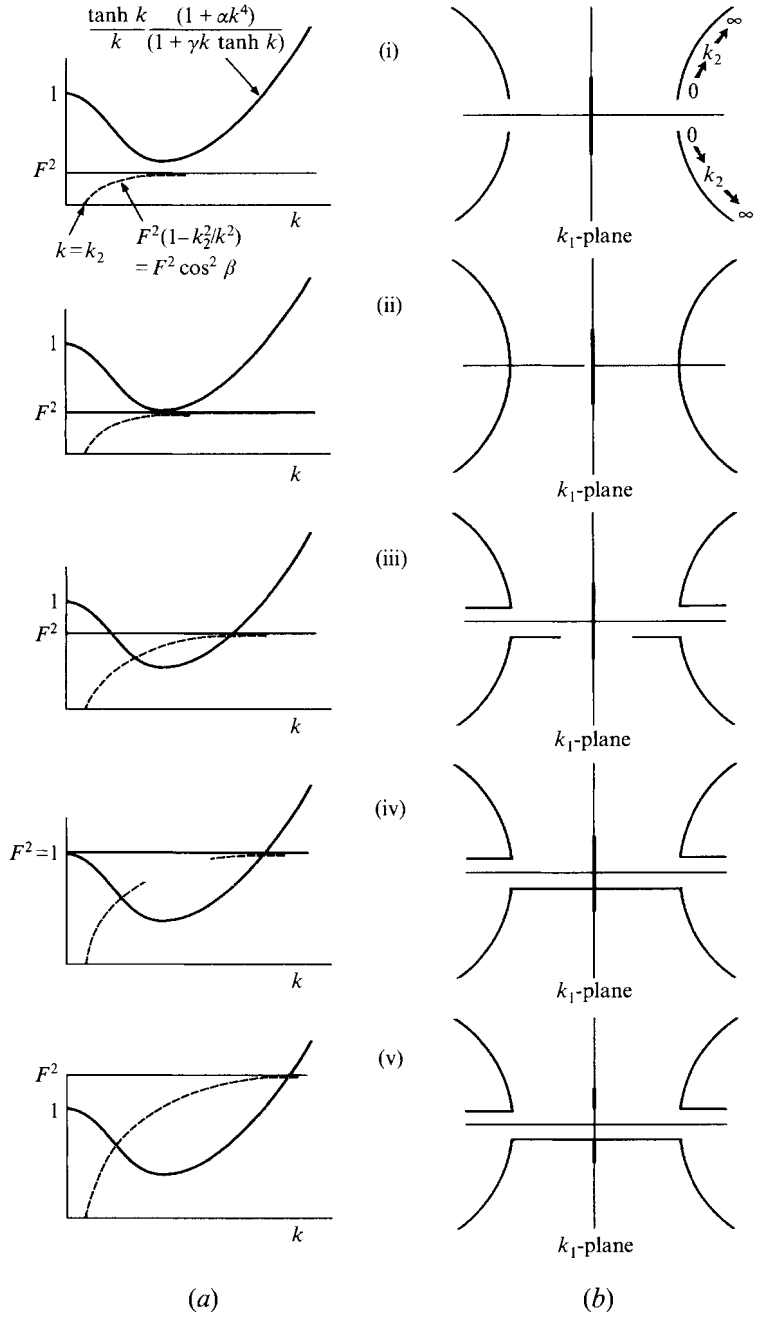


FIGURE 3. The location of the poles near the origin in the $k_1$-plane. The locations of the real poles and the two poles $\pm i(\lambda_1^2+k_2^2)^{1/2}$ are given as functions of $k_2$ for different values of $F$. The sections of the paths which are on the real axis are displaced to show the effect of the dependence on $\delta$. (*a*) The points of intersection of the curves $[\tanh k/k](1+\alpha k^4)/(1+\gamma k \tanh k)$ and $F^2(1-k_2^2/k^2)$ are given for different values of $F$. (*b*) The paths traced by the real poles and the two poles $\pm(\lambda_1^2+k_2^2)^{1/2}$ as $k_2^2$ varies from zero to infinity are given for different values of $F$.

$G_-^\delta(k_2)$ must be closed in the upper half-plane. In this case, there is also a contribution from the pole at the origin $k_1 = 0$. In front of the load $x < -a$, hence $x \pm a < 0$ and consequently both contours must be closed in the upper half-plane.

The result for $x > a$ is

$$G_-^\delta(k_2) - G_+^\delta(k_2) =$$

$$-\pi\left[4\frac{Q((B^2+k_2^2)^{1/2})}{\mathscr{D}_{k_1}^\delta(B,k_2)}\frac{\sin(aB/H)}{B}\sin\frac{xB}{H}\right.$$

$$\left.+\mathrm{i}\sum_{j=1}^{\infty}\frac{Q(\mathrm{i}\lambda_j)}{(\lambda_j^2+k_2^2)^{1/2}}\frac{(\exp[-(\lambda_j^2+k_2^2)^{1/2}(x-a)/H]-\exp[-(\lambda_j^2+k_2^2)^{1/2}(x+a)/H]}{\mathscr{D}_{k_1}^\delta(-\mathrm{i}(\lambda_j^2+k_2^2)^{1/2},k_2)}\right],$$

$$0 < k_2^2 < k_{2,c}^2$$

$$-\pi\left[2\,\mathrm{Re}\left(\frac{Q((B^2+k_2^2)^{1/2})}{\mathscr{D}_{k_1}^\delta(B,k_2)}\frac{\mathrm{e}^{\mathrm{i}B(x/H-a/H)}-\mathrm{e}^{\mathrm{i}B(x/H+a/H)}}{B}\right)\right.$$

$$\left.+\mathrm{i}\sum_{j=1}^{\infty}\frac{Q(\mathrm{i}\lambda_j)}{(\lambda_j^2+k_2^2)^{1/2}}\frac{(\exp[-(\lambda_j^2+k_2^2)^{1/2}(x-a)/H]-\exp[-(\lambda_j^2+k_2^2)^{1/2}(x+a)/H])}{\mathscr{D}_{k_1}^\delta(-\mathrm{i}(\lambda_j^2+k_2^2)^{1/2},k_2)}\right],$$

$$k_{2,c}^2 < k_2^2 < \infty, \quad (2.19)$$

where $\mathrm{Re}(z)$ denotes the real part of $z$. In the other cases, similar expressions are obtained.

For $x \neq \pm a$, it is clear that the series for $G_\pm^\delta(k_2)$ converge. For $x = \pm a$, $F \neq F_m$, and fixed $k_2$ we note that $\lambda_j \approx (j+\frac{1}{2})\pi$ as $j \to \infty$ (see figure 1*b*) and

$$\mathscr{D}_{k_1}^\delta(\mathrm{i}(\lambda_j^2+k_2^2)^{1/2},k_2) \approx 4\alpha\pi^4(j+\tfrac{1}{2})^4,$$

for large $j$. Consequently, the series converge for all values of $x$.

## 3. Approximating the integral asymptotically

The integral given by (2.17) is evaluated numerically. However, before describing the details of the method used, it is instructive to approximate (2.17) in the limit of large $|x|$ or large $b$. We concentrate on the $z = 0$ case. The details of the derivations can be found in Appendix B. Here we give only the final estimates. For $F^2 < 1$ and large $b$ and or large $|x|$, we have

$$\hat{\eta}^0 \approx \frac{P_0}{\rho g}\begin{cases}\dfrac{4Q(B_0)}{\mathscr{D}_{k_1}(B_0,0)}\dfrac{\sin(a/H)B_0}{B_0}\,\mathrm{Im}\left[\mathrm{e}^{-\mathrm{i}(x/H)B_0}\,\mathrm{erf}\left(\dfrac{b\,\mathrm{e}^{-\mathrm{i}\pi/4}}{(2HxB_0'')^{1/2}}\right)\right], & x > a; \quad (3.1a)\\[2ex] \dfrac{1}{F^2-1}+2\dfrac{Q(A_0)}{\mathscr{D}_{k_1}(A_0,0)}\dfrac{\cos((x-a)/H)A_0}{A_0}+2\dfrac{Q(B_0)}{\mathscr{D}_{k_1}(B_0,0)}\dfrac{\cos((x+a)/H)B_0}{B_0}, & \\ & -a < x < a; \quad (3.1b)\\[2ex] -\dfrac{4Q(A_0)}{\mathscr{D}_{k_1}(A_0,0)}\dfrac{\sin(a/H)A_0}{A_0}\,\mathrm{Im}\left[\mathrm{e}^{-\mathrm{i}(x/H)A_0}\,\mathrm{erf}\left(\dfrac{b\,\mathrm{e}^{-\mathrm{i}\pi/4}}{(2H|xA_0''|)^{1/2}}\right)\right], & x < -a; \quad (3.1c)\end{cases}$$

where $A_0 = A(0)$, $B_0 = B(0)$ and $\mathrm{Im}(z)$ denotes the imaginary part of $z$. By taking $x$ large with $b$ fixed in (3.1 *a*, *c*), we obtain the far-field approximations

$$\hat{\eta}^0 \approx 4b\left(\frac{2}{\pi}\right)^{1/2}\frac{P_0}{\rho g}\begin{cases} -\dfrac{Q(B_0)}{\mathscr{D}_{k_1}(B_0,0)}\dfrac{\sin(aB_0/H)}{B_0}\dfrac{\sin((x/H)B_0+\pi/4)}{(HxB_0'')^{1/2}}, & x>a; \\ \dfrac{Q(A_0)}{\mathscr{D}_{k_1}(A_0,0)}\dfrac{\sin(aA_0/H)}{A_0}\dfrac{\sin((x/H)A_0+\pi/4)}{(H|xA_0''|)^{1/2}}, & x<-a. \end{cases} \tag{3.2}$$

For $F^2 > 1$ and $b$ large, we have

$$\hat{\eta}^0 \approx \frac{P_0}{\rho g}\begin{cases} \mathrm{i}\dfrac{Q(\mathrm{i}\Lambda_0)}{\mathscr{D}_{k_1}(\mathrm{i}\Lambda_0,0)}\left[\dfrac{\mathrm{e}^{-((x-a)/H)\Lambda_0}-\mathrm{e}^{-((x+a)/H)\Lambda_0}}{\Lambda_0}\right], & x>a; \\ \dfrac{1}{F^2-1}+2\dfrac{Q(\Lambda_0)}{\mathscr{D}_{k_1}(\Lambda_0,0)}\dfrac{\cos((x-a)/H)\Lambda_0}{\Lambda_0} & \\ -\mathrm{i}\dfrac{Q(\mathrm{i}\Lambda_0)}{\mathscr{D}_{k_1}(\mathrm{i}\Lambda_0,0)}\left[\dfrac{\mathrm{e}^{((x-a)/H)\Lambda_0}+\mathrm{e}^{-((x+a)/H)\Lambda_0}}{\Lambda_0}\right], & -a\leqslant x\leqslant a; \\ -\dfrac{4Q(\Lambda_0)}{\mathscr{D}_{k_1}(\Lambda_0,0)}\dfrac{\sin(a/H)\Lambda_0}{\Lambda_0}\mathrm{Im}\left[\mathrm{e}^{-\mathrm{i}(x/H)\Lambda_0}\mathrm{erf}\left(\dfrac{b\,\mathrm{e}^{-\mathrm{i}\pi/4}}{(2H|xA_0''|)^{1/2}}\right)\right] & \\ -\mathrm{i}\dfrac{Q(\mathrm{i}\Lambda_0)}{\mathscr{D}_{k_1}(\mathrm{i}\Lambda_0,0)}\left[\dfrac{\mathrm{e}^{((x-a)/H)\Lambda_0}-\mathrm{e}^{((x+a)/H)\Lambda_0}}{\Lambda_0}\right], & x<-a; \end{cases} \tag{3.3}$$

where $\Lambda_0 = \lambda_1(0)$. The estimates given by (3.1)–(3.3) are not valid for $F^2$ near one.

The case $F^2$ near 1 is of particular interest since we wish to show that at the load speed $U_g$ there is no resonance and the ice displacement remains bounded. Again, these estimates are valid for large $b$:

$$\hat{\eta}^0 \approx \frac{P_0}{\rho g}\begin{cases} -\dfrac{4(a/H)(b/H)^{1/2}}{\pi(\frac{1}{3}+\gamma)^{3/4}}\left[\mathscr{Y}\left(\dfrac{x/H}{(\frac{1}{3}+\gamma)^{1/4}(b/H)^{1/2}}\right)-\tfrac{1}{2}\mathscr{W}\left(\dfrac{x/H}{(\frac{1}{3}+\gamma)^{1/4}(b/H)^{1/2}}\right)\right], & x>a; \\ \dfrac{1+45\alpha}{45(\frac{1}{3}+\gamma)^2}+\dfrac{2Q(A_0)\cos((x-a)/H)A_0}{\mathscr{D}_{k_1}(A_0,0)A_0}-\dfrac{1}{8(\frac{1}{3}+\gamma)}\left[3\left(\dfrac{x+a}{H}\right)^2+\left(\dfrac{x-a}{H}\right)^2\right] & \\ +\left(\dfrac{2}{\pi}\right)^{1/2}\dfrac{a/H}{(\frac{1}{3}+\gamma)^{3/4}}\left(\dfrac{b}{H}\right)^{1/2}, & -a<x<a; \\ \dfrac{4Q(A_0)}{\mathscr{D}_{k_1}(A_0,0)A_0}\sin\left(\dfrac{x}{H}A_0\right)\sin\left(\dfrac{a}{H}A_0\right)+\dfrac{2}{\pi}\dfrac{(a/H)(b/H)^{1/2}}{(\frac{1}{3}+\gamma)^{3/4}} & \\ \times\mathscr{W}\left(\dfrac{|x|/H}{(\frac{1}{3}+\gamma)^{1/4}(b/H)^{1/2}}\right), & x<-a. \end{cases} \tag{3.4}$$

The functions $\mathscr{Y}(x)$ and $\mathscr{W}(x)$ are defined in Appendix B. It can be shown that the estimate given by (3.4) is $O(1-F^2)^{1/2}$ for $F^2 < 1$ and $o(F^2-1)^{1/2}$ for $F^2 > 1$.

## 4. The numerical approximation of the integral

The integral given by (2.17) is approximated numerically using an adaptive Gaussian quadrature scheme. As was done in obtaining the asymptotic estimates of §3, we use the symmetry in $k_2$ and write (2.17) in the form

$$\int_0^\infty \sin ruR(u)\,\mathrm{d}u, \quad \text{where} \quad R(k_2) = G_-^0(k_2) - G_+^0(k_2).$$

By breaking up $[0, \infty)$ into intervals of length $\pi$, we obtain

$$\int_0^\infty \sin ruR(u)\,\mathrm{d}u = \frac{1}{r}\int_0^\pi \sin u \sum_{j=0}^{\infty}\left[R\left(\frac{u+2j\pi}{r}\right) - R\left(\frac{u+(2j+1)\pi}{r}\right)\right]\mathrm{d}u. \tag{4.1}$$

In evaluating the integrals in (4.1) the added complication of the square-root singularity at $k_{2,c}$ is handled by omitting the interval containing the singularity from the sum in (4.1) and evaluating its contribution to the integral separately. The number of terms in the sum was taken between 9 and 20.

The integral in (4.1) was approximated by using adaptive Gaussian quadrature. In this scheme, the interval of integration is bisected and an $n$-point Gauss–Legendre rule is applied over the entire interval and each subinterval. The integral over a given interval $[u_l, u_r]$ is accepted as accurate if the result of the $n$-point rule applied to $[u_l, u_r]$ and the sum of the applications of the same rule to the intervals $[u_l, (u_l+u_r)/2]$ and $[(u_l+u_r)/2, u_r]$ differs by less than $10^{-8}(u_r-u_l)$. If this condition is not met then $[u_l, u_r]$ is bisected and the procedure is repeated on each of the subintervals. In our calculations, a four-point rule was used. The number of subdivisions was limited to 20; however, this limit was never attained.

Although the above quadrature scheme can deal with the singularity at $k_{2,c}$, it does so by using a fine subdivision and, consequently, a large number of function evaluations, near this point. The efficiency of the numerical scheme was improved by treating the interval $[u_l, u_r]$ containing $k_{2,c}$ separately. This interval was partitioned into four parts $[u_l, (1-\epsilon)k_{2,c}]$, $[(1-\epsilon)k_{2,c}, k_{2,c}]$, $[k_{2,c}, (1+\epsilon)k_{2,c}]$, and $[(1+\epsilon)k_{2,c}, u_r]$. The value of $\epsilon$ was taken between 0.1 and 0.001. On the two intervals $[u_l, (1-\epsilon)k_{2,c}]$ and $[(1+\epsilon)k_{2,c}, u_r]$ the adaptive quadrature rule was applied. On the two intervals $[(1-\epsilon)k_{2,c}, k_{2,c}]$ and $[k_{2,c}(1+\epsilon)k_{2,c}]$, we used a three-point weighted Gaussian quadrature rule with weight function $1/u^{1/2}$ (see Isaacson & Keller 1966).

The most computationally intensive aspect of the calculation was the location of the poles $\lambda_j, j = 1, \ldots,$ and $A$ and $B$ as functions of $k_2$. These were computed using Newton's method on $\mathscr{D}(k_1, k_2)$, i.e. (2.14). For all values of $k_2$, it is straightforward to obtain good starting estimates for the $\lambda_j$. Hence the poles on the imaginary axis can be computed efficiently. To locate the complex poles, we continue on $k_2$. That is, values of $A$ and $B$ are computed for small $k_2$ and then used as estimates for successively larger values of $k_2$. The iteration is carried out until the iterates differed by less than $10^{-12}$ or the value of $|\mathscr{D}(k_1, k_2)|$ is less than $10^{-16}$.

The number of imaginary poles used in the series for $G_-^0(k_2) - G_+^0(k_2)$ is dependent on the value of $x$. Near $x = \pm a$ the series converges slowly and consequently more poles are required to achieve a given level of accuracy. A relative error of $10^{-6}$ is used to decide whether convergence has been achieved. Typically, the number of imaginary poles used is fewer than 10 when $|(x \pm a)/H| > 3$ and as large as 100 at $x \to \pm a$.

Varying the order of the Gauss–Legendre rule or the allowable depth of subdivisions made no significant difference in the results.

It should be noted that the integral in (2.17) can be evaluated using the fast-Fourier transform. For $F^2 < F_m^2$ this method gives good results and was used as a check. Unfortunately, for $F^2 > F_m^2$ the number of points required to obtain the necessary resolution makes the method unattractive.

Our numerical scheme gives an accurate and detailed description of the ice deflection over the entire flow field for all load speeds not equal to $U_m$. Although other numerical methods (finite difference, finite element, etc.) could be used to approximate the solution of this problem, there are a number of advantages to our approach. First, the analysis of the singularity structure of the integrand leads to a great deal of insight into the physical nature of the solution. Error estimates are easily obtained and indeed are used to ensure accurate approximations to the solution. The usual problems associated with the infinite domain are handled by the Fourier transform. Furthermore, the solution need only be computed at points where solution values are required. Finally, for a given load speed, the poles of the integrand of the Fourier integral are independent of the field point where the solution is being evaluated. Hence, the computation can be carried out efficiently.

## 5. Numerical results

Here, we give a number of results which illustrate the nature of the solution. In all of our calculations the density of the ice was taken to be $\rho' = 900$ kg m$^{-3}$.

To check the accuracy of the calculation, a comparison of the numerical approximation to the solution and the far-field approximation of the solution given by (3.2) is made. The parameters are those given by Davys *et al.* (1985) for McMurdo Sound, Antarctica. That study was undertaken to determine whether the ice of McMurdo Sound is capable of supporting fully loaded transport aircraft such as the C-130H Hercules. For our calculations the pressure supporting the aircraft was taken to be distributed uniformly over a rectangular base with $a = 1.5$ m and $b = 2.5$ m†. Figure 4 shows the results. As is to be expected the asymptotic approximation is very good for the elastic waves in front of the load. Behind the load the gravity waves are not as well approximated. A further check on the accuracy was made by comparing the numerical approximation to the solution to the large-$b$ estimates given by (3.1), (3.3) and (3.4). Figure 5 shows the results for $F^2 = 1$.

Figure 6 shows the deflection of the ice sheet in a cross-section parallel to the $x$-axis ($z = 1$) for load speed and ice/water parameters given by Takizawa (1985). For comparison the experimental and numerical results are superposed. The agreement is not very good near the critical speed $U_m$. Unlike the observed profiles, the computed profiles are symmetric about the origin for subcritical speeds. The model used in this article precludes asymmetric solutions for subcritical speeds. The symmetric placement of the complex roots $A$ and $B$ for subcritical speeds forces the solutions to be symmetric about the centre of the load. The symmetry is broken by the appearance of the real roots at the critical speed. Several authors (Takizawa 1985; Schulkes *et al.* 1988) have speculated that the asymmetry is a viscoelastic effect. Hosking *et al.* (1988) use a two-parameter memory function to model the viscoelasticity of an ice sheet and reproduce the observed lag for a line load. The maximum deflections measured by Takizawa (1985) and the maximum computed deflections agree well. Apart from the lag between the central depression and the load, the shape of the computed ice deflection profiles falls into the five stages of development described by Takizawa (1985).

† The pressure distribution on the ground which supports an aircraft is neither uniform nor rectangular. A uniform pressure distribution with these dimensions is taken only as an approximation.

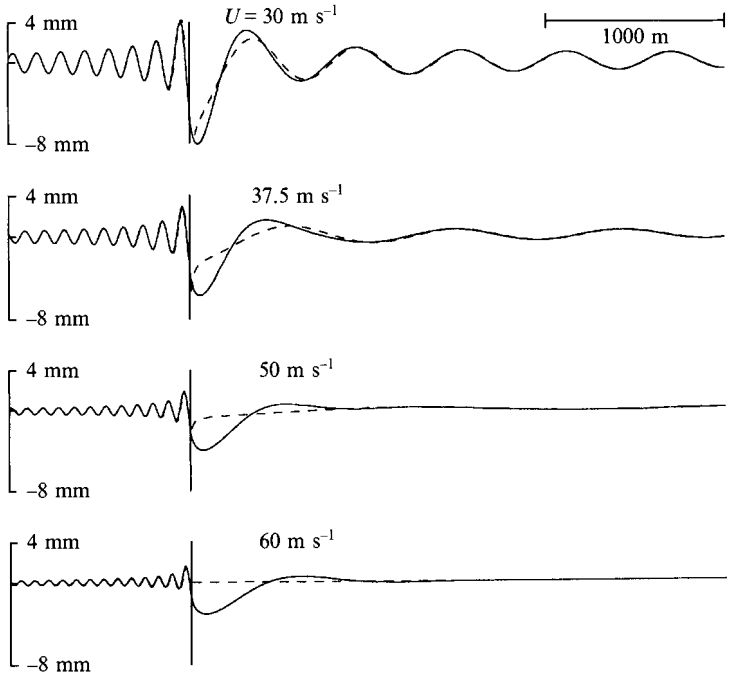


FIGURE 4. A comparison of the numerical and the far-field solution for $z = 0$. The parameters are taken from McMurdo Sound, Antarctica, $P_o = 32689$ N m$^{-2}$, $H = 350$ m, $h = 2.5$ m, $E = 5 \times 10^9$, $\sigma = 1/3$, $\rho = 10^3$ kg m$^{-3}$ as given in Davys *et al.* (1985) with $a = 1.5$ m and $b = 2.5$ m. The solid curve shows the numerical approximation to the solution. The dashed curves show the far-field estimates.

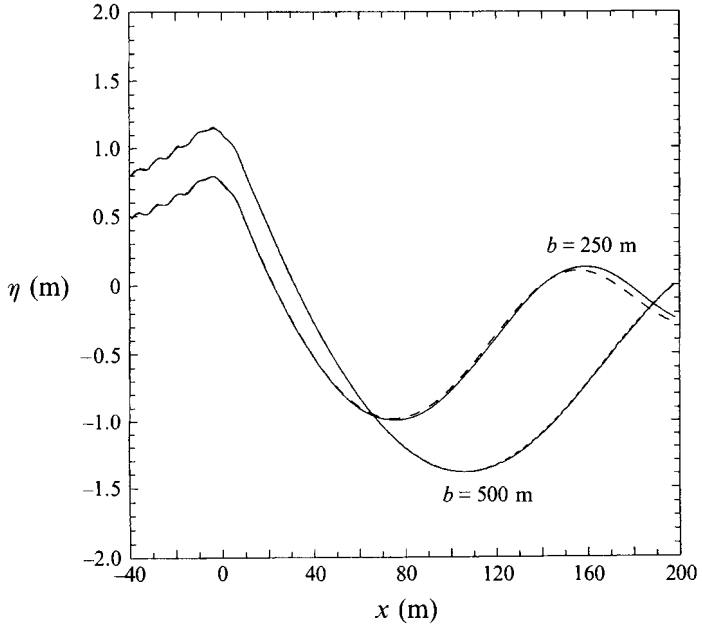


FIGURE 5. A comparison of the numerical approximation to the solution with the large-$b$ estimates. The parameters are $a = 10$, $H = 10$, $P_o = 1000$ N m$^{-2}$, $E = 5 \times 10^9$, $\sigma = 1/3$, $\rho = 10^3$ kg m$^{-3}$. $F^2 = 1$. For $b = 250$ the numerical approximation to the solution is given by the solid line, the asymptotic approximation is given by dashed line. For $b = 500$ the numerical approximation to the solution is given by the long dashes, the asymptotic approximation is given by the short dashes.

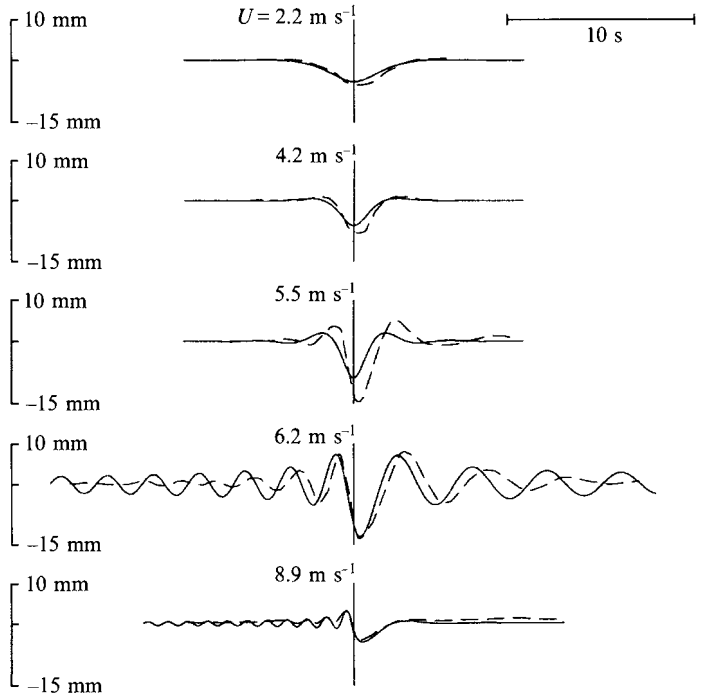


FIGURE 6. Ice deflection as a function of $x$ for different load speeds for $z = 1$. The ice parameters are $P_o = 1023.6$ N m$^{-2}$, $H = 6.8$ m, $h = 0.175$ m, $E = 5 \times 10^8$ N m$^{-2}$, $\sigma = 1/3$, $\rho = 1026$ kg m$^{-3}$, $a = 1.23$ m and $b = 0.468$ m as given in Takizawa (1985). The solid curve shows the numerical results. The dashed curve shows the experimental observations of Takizawa (1985).

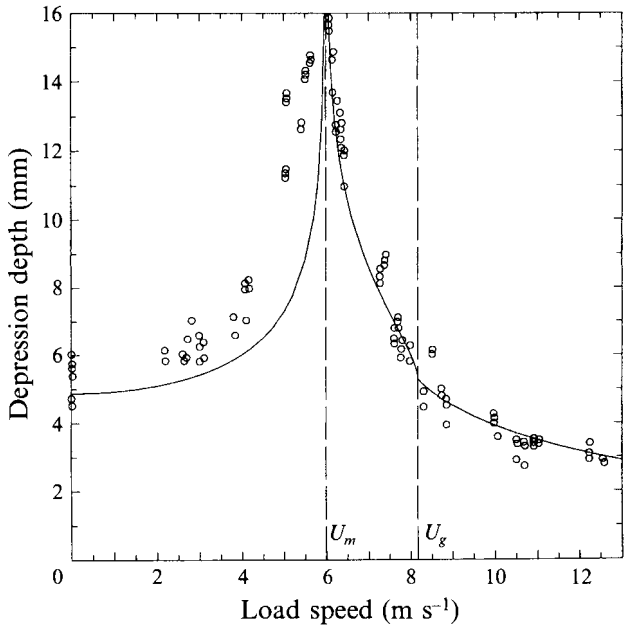


FIGURE 7. Depression depth as a function of load speed for $z = 1$. The parameters are $P_o = 1023.6$ N m$^{-2}$, $H = 6.8$ m, $h = 0.175$ m, $E = 5 \times 10^8$ N m$^{-2}$, $\sigma = 1/3$, $\rho = 1026$ kg m$^{-3}$, $a = 1.23$ m and $b = 0.468$ m as given in Takizawa (1985). The computed results are given by the solid curve, the experimental measurements of Takizawa (1985) are given by the circles.

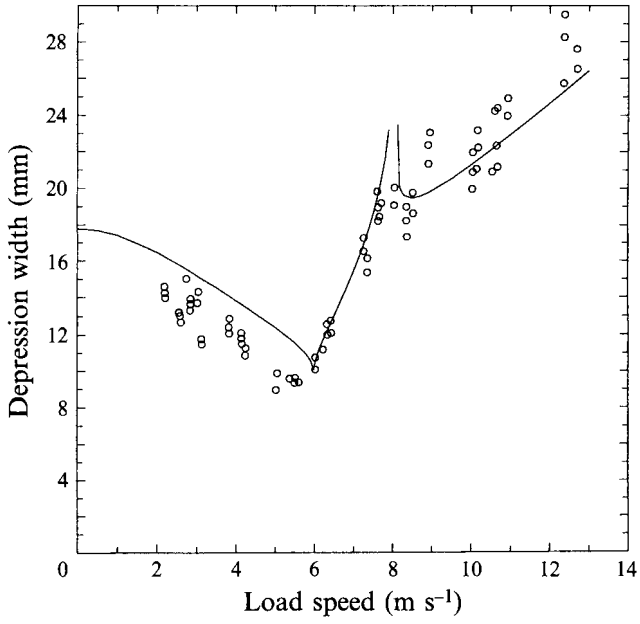


FIGURE 8. The width of the maximum depression as a function of load speed. This width is defined as the width of the largest depression measured between two consecutive points where the deflection is zero. The circles are measurements taken from Takizawa (1985). The ice parameters are $z = 1$, $P_o = 1023.6$ N m$^{-2}$, $H = 6.8$ m, $h = 0.175$ m, $E = 5 \times 10^8$ N m$^{-2}$, $\sigma = 1/3$, $\rho = 1026$ kg m$^{-3}$, $a = 1.23$ m and $b = 0.468$ m as given in Takizawa (1985).

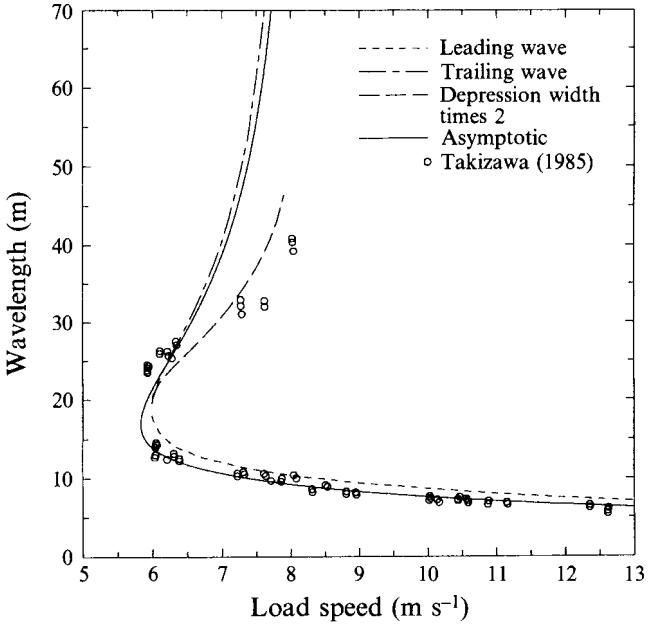


FIGURE 9. The wavelength of the leading and trailing waves as a function of load speed. The ice parameters are $z = 1$, $P_o = 1023.6$ N m$^{-2}$, $H = 6.8$ m, $h = 0.175$ m, $E = 5 \times 10^8$ N m$^{-2}$, $\sigma = 1/3$, $\rho = 1026$ kg m$^{-3}$, $a = 1.23$ m and $b = 0.468$ m as given in Takizawa (1985).

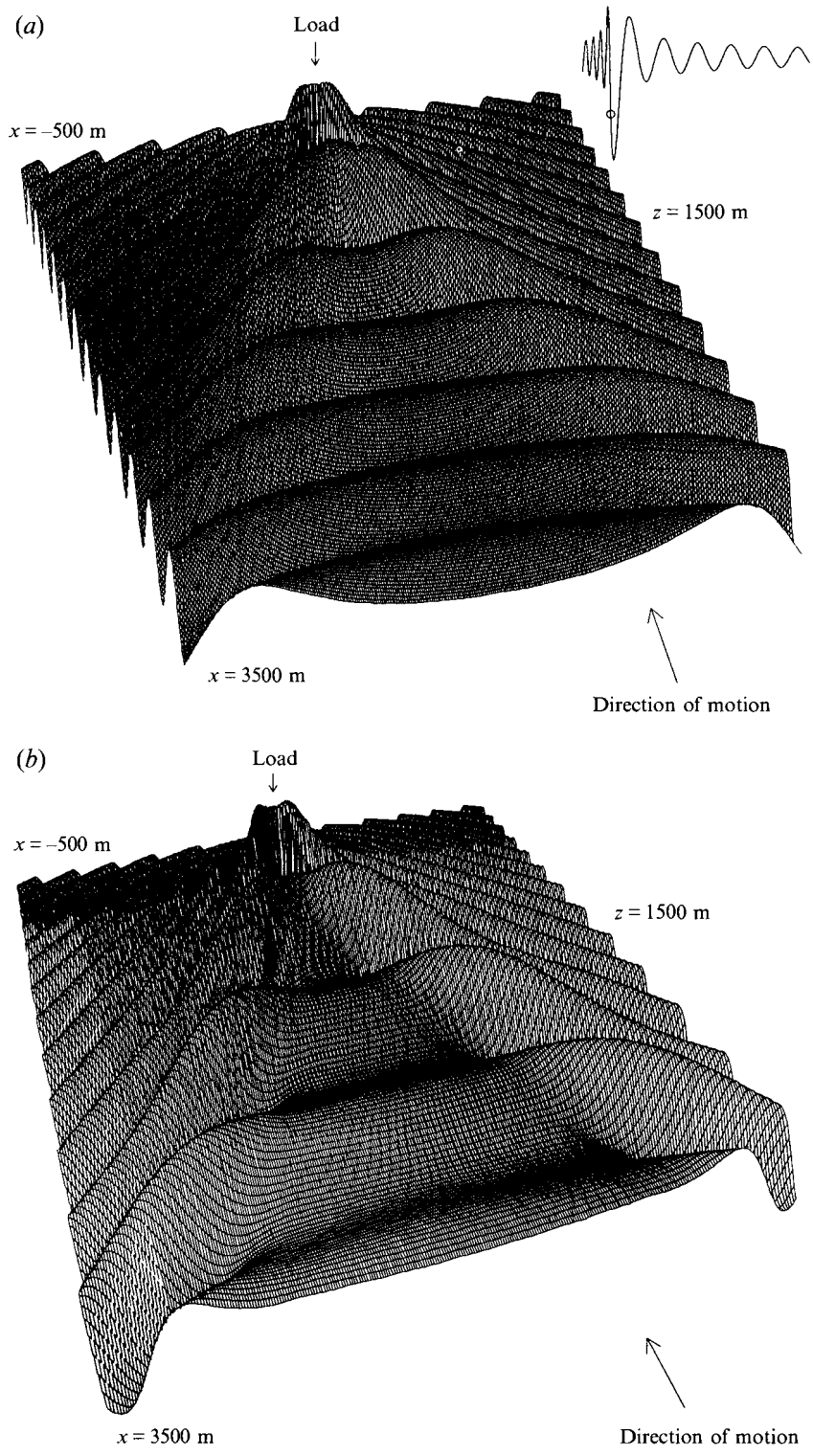


FIGURE 10 (*a*, *b*). For caption see facing page.

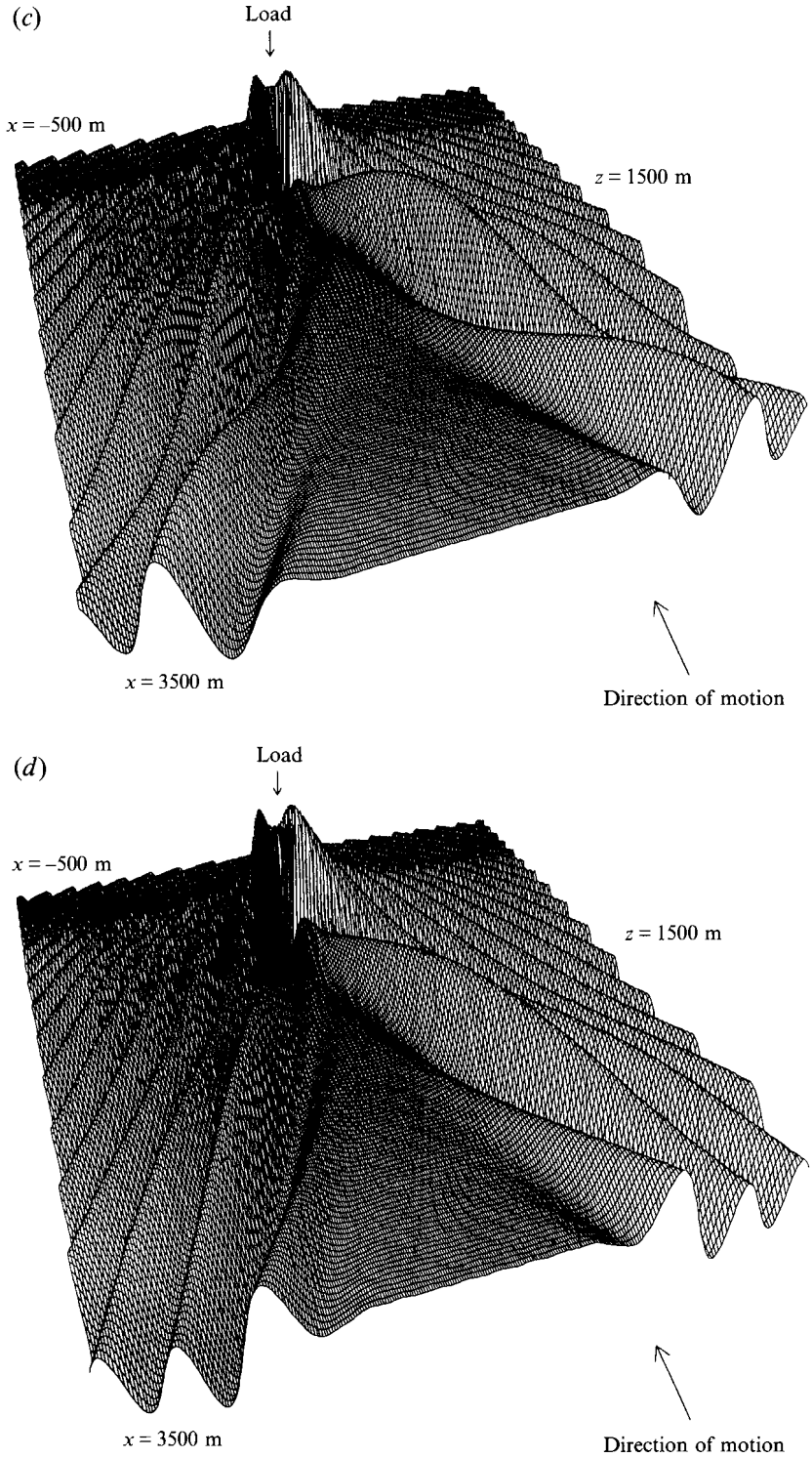


FIGURE 10. Wave surface plots as a function of $(x, z)$ for different load speeds. The ice parameters are $P_o = 1000$ N m$^{-2}$, $H = 350$ m, $h = 2.5$ m, $E = 5 \times 10^9$, $\sigma = 1/3$, $\rho = 10^3$ kg m$^{-3}$ as given in Davys *et al.* (1985). Here, $a = 10$ and $b = 20$. The speeds given in m s$^{-1}$ are: (*a*) $U = 30$, (*b*) $U = 37.5$, (*c*) $U = 50$, and (*d*) $U = 60$. The curve at the top right in (*a*) shows the ice displacement along $z = 0$. The circle indicates the position of the load.

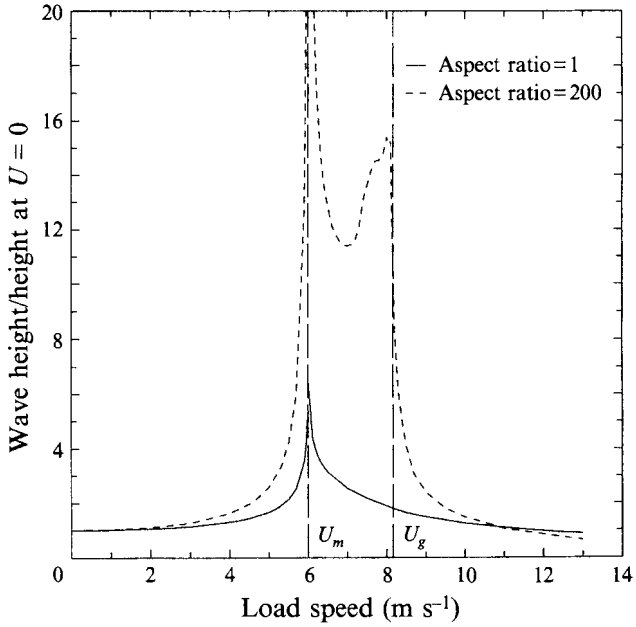


FIGURE 11. Wave height/height at $U = 0$ as a function of load speed. The parameters are $z = 0$, $H = 6.8$ m, $h = 0.175$ m, $E = 5 \times 10^8$, $\sigma = 1/3$, $\rho = 1026$ kg m$^{-3}$; $U_m = 5.99$ m s$^{-1}$, $U_g = 8.17$ m s$^{-1}$. (*a*) Aspect ratio = 1, $b = a$; (*b*) aspect ratio = 200, $b = 200a$. The wave height is taken to be the maximum displacement minus the minimum displacement. —, Aspect ratio = 1; – –, aspect ratio = 200.

Figure 7 shows the variation of maximum negative deflection with load speed. Superimposed are the experimental measurements of Takizawa (1985). The qualitative agreement between theory and experiment is good. As expected, there is a quantitative difference between the analytic and the experimental results near the critical speed. As the speed of the load increases to the critical value, the computed displacements increase more rapidly than the displacements measured by Takizawa (1985). However, for speeds greater than the critical speed the agreement is quite good.

In figure 8, we compare the computed width of the maximum depression to that measured by Takizawa (1985). Depression width is defined as the distance between the two $\eta = 0$ points which bracket the deepest depression. For speeds greater than $U_m$ the agreement is good. For speeds less than $U_m$ the computed results overestimate the measured widths. The large computed widths near $U = 8$ are an indication of the difficulty in determining the depression width as the amplitude of a wavecrest decreases to zero.

In figure 9, we compare the computed wavelengths of both the elastic and the gravity waves at different load speeds to those measured by Takizawa (1985). The computed wavelengths of the leading elastic waves are in good agreement with the measured wavelengths. Near the critical speed the agreement between the computed and measured wavelengths is very good. Schulkes *et al.* (1988) explain the discrepancy at larger wavelengths as a time-dependent effect, where insufficient time has elapsed for a complete wavelength to be propagated. Also shown for comparison is twice the width of the depression immediately behind and near the load.

Figure 4 shows the ice deflection at four supercritical speeds for the McMurdo Sound data (for these parameters $U_m = 22.5$ m s$^{-1}$). Figure 10 illustrates the ice surface

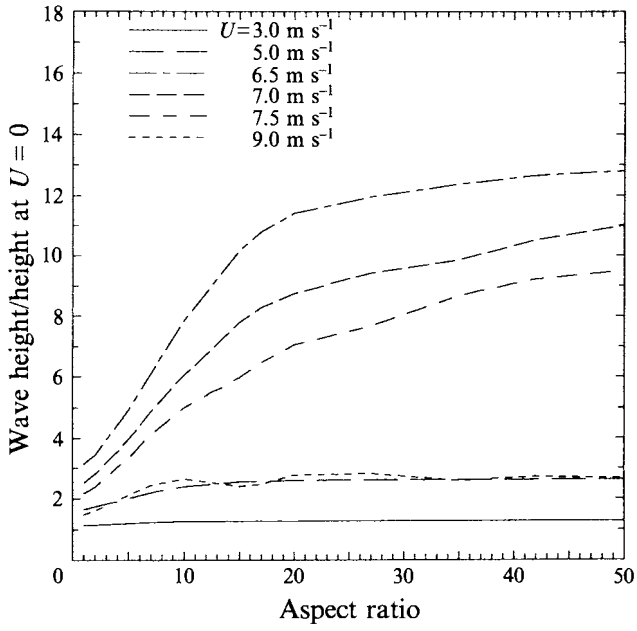


FIGURE 12. Wave height/height at $U = 0$ as a function of aspect ratio for different wave speeds. The parameters are $z = 0$, $H = 6.8$ m, $h = 0.175$ m, $E = 5 \times 10^8$, $\sigma = 1/3$, $\rho = 1026$ kg m$^{-3}$.

for the same load speeds. The surface plots show very clearly the development of the quiescent zone and the cusps behind the load. These figures show that the ice deflection changes most rapidly behind the load.

The analysis of §3 suggests that the amplitude of the steady deflection of an ice sheet increases as $b/H$ when the load speed is near $(gH)^{1/2}$. In order to investigate the effect of aspect ratio of the load on ice displacement, we computed ice deflection as a function of load speed for two different loads, one with an aspect ratio of $b/a = 1$, the other with an aspect ratio of 200. All other parameters are taken as in Takizawa (1985). Figure 11 provides a summary of the results. It is clear that the influence of aspect ratio is significant but limited to speeds between $U_m$ and $U_g$. Figure 12 shows the dependence of ice deflection normalized on the deflection induced by the same load at zero speed for a number of load speeds. It should be noted that for load speeds near the critical speed the amplification of the deflection over the deflection of a stationary load increases most rapidly as the aspect ratio increases from 1 to 20. Figure 13 shows the surface plot of the ice deflection for a load of dimension $a = 10$ m by $b = 200$ m for the parameters of McMurdo Sound. This figure should be compared to figure 10(*a*). For wide loads the surface deflection has much more structure than does the surface displacement corresponding to loads of smaller aspect ratios.

## 6. Conclusions

In this article, we have investigated the steady response of a uniform ice sheet of infinite extent which is supported by water of constant depth. The deflection is assumed to be produced by the steady motion of a uniform, rectangular pressure distribution. The solution is expressed as a two-dimensional Fourier integral. An analysis of the poles of the integrand is used to obtain asymptotic estimates for the ice deflection in

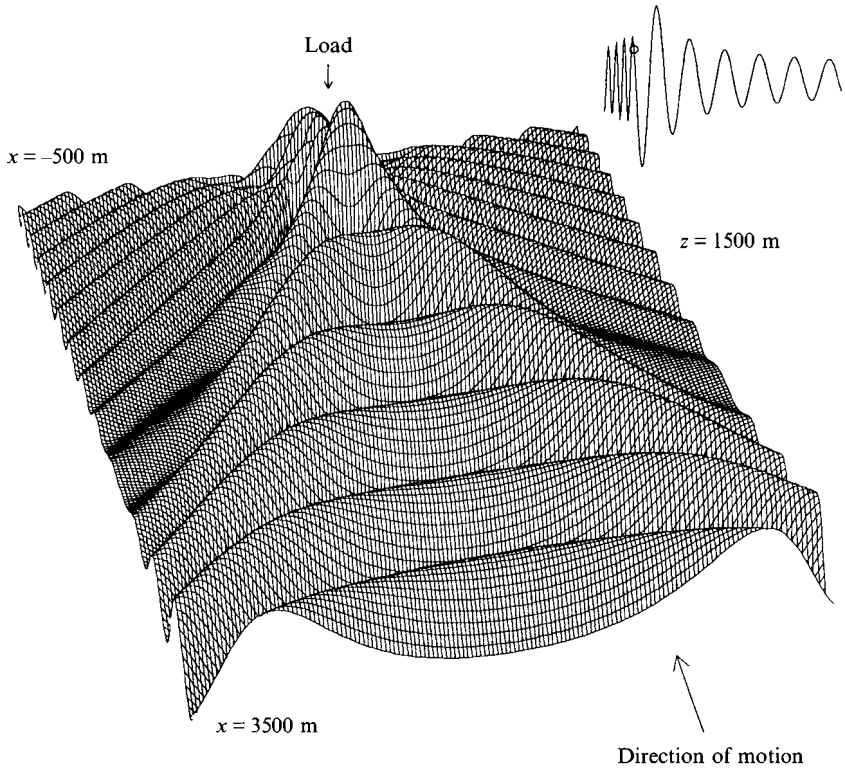


FIGURE 13. Wave surface plot as a function of $(x, z)$ for different load speeds with $b$ large. The ice parameters are $P_o = 1000\ \mathrm{N\ m^{-2}}$, $H = 350$ m, $h = 2.5$ m, $E = 5 \times 10^9$, $\sigma = 1/3$, $\rho = 10^3\ \mathrm{kg\ m^{-3}}$ as given in Davys *et al.* (1985). Here, $a = 10$, $b = 200$, and $U = 30\ \mathrm{m\ s^{-1}}$. The curve at the top right shows the ice displacement along $z = 0$. The circle indicates the position of the load.

the limit of large $|x|$ or large $b$. In addition, the integral is approximated numerically using the method of residues together with a simple adaptive quadrature scheme. Using this numerical scheme the problem of an infinite computational domain is eliminated. Moreover, the solution need only be computed where solution values are required.

Our analysis shows that no steady-state solution is possible when the load speed equals the minimum speed of the elastic waves of the ice. This result supports the analysis given by Davys *et al.* (1985). However, a steady solution does exist when load speed equals $(gH)^{1/2}$. However, as is the case for the line load (Schulkes & Sneyd 1988), it is possible that such steady solutions are not realizable since solutions of the initial value problem may grow with time.

Our calculations suggest a strong dependence of the amplitude of the ice deflection on the aspect ratio of the load when the load speed is between $U_m$ and $U_g$.

The results of our calculations are in good agreement with the experimental observations of Takizawa (1985).

The authors would like to acknowledge the support received in the initial stages of this work from J. E. Laframboise of the Transportation Development Centre, Transport Canada. The first author would like to thank Professor R. Hosking for discussions which brought out the relationship between this work and that which appears in Schulkes *et al.* (1987) and for making a number of helpful comments on the

organization of this article. We would also like to thank the anonymous referees for a number of constructive comments.

## Appendix A

In this appendix, we analyse the form of the singularities which occur in the integrand of (2.17). We stress that the position of each pole in the $k_1$-integral depends on the value of $k_2$. This dependency is given implicitly by (2.14). We let $k_{1,c}$ and $k_{2,c}$ be the values of $k_1$ and $k_2$, respectively, at which the real poles coalesce and suppose that $k_{2,c}^2 \neq 0$. Since two real poles coalesce then separate as a complex-conjugate pair, it is necessary that $\mathscr{D}(k_{1,c}, k_{2,c}) = \mathscr{D}_{k_1}(k_{1,c}, k_{2,c}) = 0$. Expanding $\mathscr{D}(k_1, k_2)$ about the critical point and keeping terms up to the second order, we obtain

$$0 = \mathscr{D}_{k_2}(k_2 - k_{2,c}) + \tfrac{1}{2}[\mathscr{D}_{k_1,k_1}(k_1 - k_{1,c})^2 + 2\mathscr{D}_{k_1,k_2}(k_1 - k_{1,c})(k_2 - k_{2,c}) + \mathscr{D}_{k_2,k_2}(k_2 - k_{2,c})^2)]. \tag{A 1}$$

Solving for $k_1$ in terms of $k_2$ and keeping only the lowest-order term results in the expressions

$$k_1(k_2) = k_{1,\pm}(k_2) \approx k_{1,c} \pm \left[2\frac{\mathscr{D}_{k_2}}{\mathscr{D}_{k_1,k_1}}(k_{2,c} - k_2)\right]^{1/2}, \tag{A 2}$$

where all derivatives are evaluated at $(k_{1,c}, k_{2,c})$ and $k_{1,\pm}(k_2)$ represent the two branches of the curve given by (2.14). It is easy to check that the sign of the partials of $\mathscr{D}$, evaluated at $(k_{1,c}, k_{2,c})$, are such that the argument of the square root is positive for $|k_2| < |k_{2,c}|$ and negative otherwise. In this notation, the integrand of (2.11) takes the form

$$\frac{\mathscr{Q}(k_1^2, k_2^2)}{(k_1^2 - k_{1,-}^2(k_2))(k_1^2 - k_{1,+}^2(k_2))}. \tag{A 3}$$

Here, $\mathscr{Q}$ is used to denote the part of the integrand of (2.11) which is regular at the poles $k_1^2 = k_{1,\pm}^2(k_2)$. Using the approximation given by (A 2) in the residue of (A 3) at $k_{1,\pm}(k_2)$, it is easy to see that for values of $k_2$ close to $k_{2,c}$, the residue is proportional to

$$\frac{1}{8k_{1,c}}\frac{\mathscr{Q}(k_{1,c}^2, k_{2,c}^2)}{[2(\mathscr{D}_{k_2}/\mathscr{D}_{k_1,k_1})(k_2 - k_{2,c})]^{1/2}}.$$

Hence for $k_{2,c} \neq 0$, the singularity in the $k_2$-integral at $k_2 = k_{2,c}$ is integrable. At the critical speed $U_m$, $k_{2,c} = 0$, $\mathscr{D}_{k_2} = \mathscr{D}_{k_1,k_2} = 0$ and $\mathscr{D}_{k_1,k_1}\mathscr{D}_{k_2,k_2} > 0$. It follows that

$$k_1(k_2) = k_{1,\pm}(k_2) \approx k_{1,c} \pm \mathrm{i}(\mathscr{D}_{k_2,k_2}\mathscr{D}_{k_1,k_1})^{1/2}|k_2|.$$

The singularity is of the form $1/|k_2|$ and the integral is no longer finite.

It remains to consider what happens for small $k_2^2$ when $F = 1$. In this case there are four roots near the origin of the $k_1$-plane. Since $k$ is small, we can expand $\tanh k$ about zero in (3.1). To lowest order in $k_2$, we find that the roots of (2.14) are

$$k_1^2 = \pm\frac{|k_2|}{(\gamma + \frac{1}{3})^{1/2}} + O(k_2^2). \tag{A 4}$$

Using this estimate in $Q(k)/\mathscr{D}(k_1, k_2)$ it is easy to show that, to lowest order, the residue from these poles is proportional to

$$\frac{1}{(\frac{1}{3}+\gamma)^{3/4}|k_2|^{1/2}}.$$

Consequently, the contribution of these four poles to the $k_2$-integral is finite.

## Appendix B

In this Appendix we outline the details of the derivations of the estimates given in §3 to (2.17) in the limit of large $|x|$ or large $b$. Only the case $z = 0$ is considered. For large $b$ and or large $|x|$, the major contribution to the integral in (2.17) comes from an interval about $k_2 = 0$. Since the poles $B$ and $-\bar{B}$ coalesce at $F^2 = 1$, it is necessary to consider the cases $F^2 < 1$ and $F^2 > 1$ separately. For $F^2 < 1$, the exponential terms in (2.19) do not contribute to the leading term. Consequently, for $x > a$, we have the approximation

$$\hat{\eta}^0 \approx -\frac{4P_0}{\pi\rho g}\int_{-\infty}^{\infty} \frac{Q((B(k_2)^2+k_2^2)^{1/2})}{\mathscr{D}_{k_1}(B(k_2), k_2)} \frac{\sin bk_2/H}{k_2} \sin\left(\frac{a}{H}B(k_2)\right) \frac{\sin(x/H)\,B(k_2)}{B(k_2)}\,\mathrm{d}k_2, \quad \text{(B 1)}$$

where the dependence of $B$ on $k_2$ has been shown explicitly. An estimate for (B 1) is obtained by expanding $B(k_2)$ about $k_2 = 0$ and retaining only second order terms. The leading term of the approximation is given by

$$\hat{\eta}^0 \approx \frac{4P_0}{\pi\rho g}\frac{Q(B_0)}{\mathscr{D}_{k_1}(B_0, 0)} \frac{\sin(a/H)\,B_0}{B_0} \operatorname{Im}\left[\int_{-\infty}^{\infty} \frac{\sin bk_2/H}{k_2} \exp[-\mathrm{i}\,x/H(B_0+\tfrac{1}{2}B_0''k_2^2)]\,\mathrm{d}k_2\right]. \quad \text{(B 2)}$$

On evaluating the integral in (B 2), we arrive at the estimate given by (3.1 *a*). To obtain (3.1 *b*, *c*) similar calculations can be carried out for $x < -a$ and $-a < x < a$ by using (2.17) together with (2.18) written for the corresponding interval in $x$.

The solution for a line load can be recovered by taking $b \gg xB_0''$ and $b \gg |xA_0''|$ in (3.1 *a*) and (3.1 *c*) respectively to obtain

$$\hat{\eta}^0 \approx 4b\frac{P_0}{\rho g}\begin{cases} -\dfrac{Q(B_0)}{\mathscr{D}_{k_1}(B_0, 0)} \dfrac{\sin aB_0/H}{B_0} \sin\left(\dfrac{x}{H}B_0\right), & x > a, \\ \dfrac{Q(A_0)}{\mathscr{D}_{k_1}(A_0, 0)} \dfrac{\sin aA_0/H}{A_0} \sin\left(\dfrac{x}{H}A_0\right), & x < -a. \end{cases} \quad \text{(B 3)}$$

For $F^2 > 1$, similar calculations to those used to arrive at (3.1) give (3.3). Clearly, the estimates given by (3.1) and (3.3) are not valid for $F^2$ near one.

For $F^2 \approx 1$ and large $b$, the major contribution to the ice displacement comes from the real poles $A$ and $B$ and the exponential terms in $(\lambda_1^2+k_2^2)^{1/2}$ for $k_2$ small. Consequently, it is necessary to obtain estimates for $B$ and $(\lambda_1^2+k_2^2)^{1/2}$ for small $k_2$ and small $1-F^2$. These are obtained by approximating $\tanh k$ in (2.14) for small $k$ and solving the resulting quadratic for $k^2$. For $F^2 = 1$, the leading term in the approximation for $k_1$ is given by (A 4).

For convenience, we write (2.17) as

$$\hat{\eta}^0 \approx \frac{2P_0}{\pi\rho g}\int_0^{\infty} \frac{\sin bk_2/H}{k_2} \mathscr{R}(k_2; F^2)\,\mathrm{d}k_2. \quad \text{(B 4)}$$

The dependence of $A$, $B$ and $\lambda_1$ on $F^2$ is emphasized by its appearance as an argument of $\mathscr{R}$. To approximate (B 4) as $F^2 \to 1$ with large, fixed $b$, we write

$$\hat{\eta}^0 \approx \frac{2P_0}{\pi\rho g}\left[\int_0^\infty \frac{\sin bk_2/H}{k_2}\mathscr{R}(k_2;1)\,\mathrm{d}k_2 + \int_0^\infty \frac{\sin bk_2/H}{k_2}[\mathscr{R}(k_2;F^2)-\mathscr{R}(k_2;1)]\,\mathrm{d}k_2\right]. \tag{B 5}$$

For $-a < x < a$, we have

$$\mathscr{R}(k_2;F^2) = 2\frac{Q((B^2+k_2^2)^{1/2})}{B}\frac{\cos((x+a)/HB)}{\mathscr{D}_{k_1}(B,k_2)} + 2\frac{Q((A^2+k_2^2)^{1/2})}{A}\frac{\cos((x-a)/HA)}{\mathscr{D}_{k_1}(A,k_2)}$$

$$-\frac{1}{1+\alpha k_2^4} - i\frac{Q(\mathrm{i}\lambda_1)}{(\lambda_1^2+k_2^2)^{1/2}}\left[\frac{\exp[+(\lambda_1^2+k_2^2)^{1/2}(x-a)/H]+\exp[-(\lambda_1^2+k_2^2)^{1/2}(x+a)/H]}{\mathscr{D}_{k_1}(\mathrm{i}(\lambda_1^2+k_2^2)^{1/2},k_2)}\right].$$

For $F^2 < 1$, we find that

$$\begin{aligned}\hat{\eta}^0 &\approx \frac{P_0}{\rho g}\left[\frac{1+45\alpha}{45(\frac{1}{3}+\gamma)^2} + \frac{2Q(A_0)\cos((x-a)/HA_0)}{\mathscr{D}_{k_1}(A_0,0)A_0} - \frac{1}{8(\frac{1}{3}+\gamma)}\left[3\left(\frac{x+a}{H}\right)^2+\left(\frac{x-a}{H}\right)^2\right]\right.\\ &\quad +\left(\frac{2}{\pi}\right)^{1/2}\frac{a/H}{(\frac{1}{3}+\gamma)^{3/4}}\left(\frac{b}{H}\right)^{1/2} - \frac{\sqrt{2}}{\pi}\frac{a}{H}\frac{b}{H}\frac{F^2(1-F^2)^{1/2}}{(\frac{1}{3}+\gamma)}\\ &\quad \left.\times\int_0^\infty \frac{u((1+u^4)^{1/2}-1)^{1/2}-(1+u^4)^{1/2}}{(1+u^4)^{1/2}}\,\mathrm{d}u\right]\\ &\approx \frac{P_0}{\rho g}\left[\frac{1+45\alpha}{45(\frac{1}{3}+\gamma)^2} + \frac{2Q(A_0)\cos((x-a)/HA_0)}{\mathscr{D}_{k_1}(A_0,0)A_0} - \frac{1}{8(\frac{1}{3}+\gamma)}\left[3\left(\frac{x+a}{H}\right)^2+\left(\frac{x-a}{H}\right)^2\right]\right.\\ &\quad \left.+\left(\frac{2}{\pi}\right)^{1/2}\frac{a/H}{(\frac{1}{3}+\gamma)^{3/4}}\left(\frac{b}{H}\right)^{1/2} - \frac{2}{\pi}\frac{a}{H}\frac{b}{H}\frac{F^2(1-F^2)^{1/2}}{(\frac{1}{3}+\gamma)}\right].\end{aligned} \tag{B 6}$$

For $F^2 > 1$,

$$\begin{aligned}\hat{\eta}^0 &\approx \frac{P_0}{\rho g}\left[\frac{1+45\alpha}{45(\frac{1}{3}+\gamma)^2} + \frac{2Q(A_0)\cos((x-a)/HA_0)}{\mathscr{D}_{k_1}(A_0,0)A_0} - \frac{1}{8(\frac{1}{3}+\gamma)}\left[3\left(\frac{x+a}{H}\right)^2+\left(\frac{x-a}{H}\right)^2\right]\right.\\ &\quad +\left(\frac{2}{\pi}\right)^{1/2}\frac{a/H}{(\frac{1}{3}+\gamma)^{3/4}}\left(\frac{b}{H}\right)^{1/2} - \frac{\sqrt{2}}{\pi}\frac{a}{H}\frac{b}{H}\frac{F^2(1-F^2)^{1/2}}{(\frac{1}{3}+\gamma)}\\ &\quad \left.\times\int_0^\infty \frac{u((1+u^4)^{1/2}+1)^{1/2}-(1+u^4)^{1/2}}{(1+u^4)^{1/2}}\,\mathrm{d}u\right]\\ &\approx \frac{P_0}{\rho g}\left[\frac{1+45\alpha}{45(\frac{1}{3}+\gamma)^2} + \frac{2Q(A_0)\cos((x-a)/HA_0)}{\mathscr{D}_{k_1}(A_0,0)A_0} - \frac{1}{8(\frac{1}{3}+\gamma)}\left[3\left(\frac{x+a}{H}\right)^2+\left(\frac{x-a}{H}\right)^2\right]\right.\\ &\quad \left.+\left(\frac{2}{\pi}\right)^{1/2}\frac{a/H}{(\frac{1}{3}+\gamma)^{3/4}}\left(\frac{b}{H}\right)^{1/2}\right].\end{aligned} \tag{B 7}$$

For $x > a$, we have

$$\mathscr{R}(k_2;F^2) = -4\frac{Q((B^2+k_2^2)^{1/2})}{\mathscr{D}_{k_1}(B,k_2)}\frac{\sin(a/H)B}{B}\sin\frac{x}{H}B$$

$$+\mathrm{i}\frac{Q(\mathrm{i}\lambda_1)}{(\lambda_1^2+k_2^2)^{1/2}}\left[\frac{\exp[+(\lambda_1^2+k_2^2)^{1/2}(x-a)/H]-\exp[-(\lambda_1^2+k_2^2)^{1/2}(x+a)/H]}{\mathscr{D}_{k_1}(\mathrm{i}(\lambda_1^2+k_2^2)^{1/2},k_2)}\right].$$

The contribution to the leading term of the first integral of (B 5) comes from the poles $B(k_2)$ and $\lambda_1(k_2)$. The result is

$$\hat{\eta}^0 \approx -\frac{4P_0}{\pi\rho g}\frac{(a/H)(b/H)^{1/2}}{(\frac{1}{3}+\gamma)^{3/4}}\left[\mathscr{Y}\left(\frac{x/H}{(\frac{1}{3}+\gamma)^{1/4}(b/H)^{1/2}}\right)-\tfrac{1}{2}\mathscr{W}\left(\frac{x/H}{(\frac{1}{3}+\gamma)^{1/4}(b/H)^{1/2}}\right)\right] \quad \text{(B 8)}$$

where

$$\mathscr{Y}(x) = \int_0^\infty \frac{\sin w^2}{w^2}\sin xw\,\mathrm{d}w$$

and

$$\mathscr{W}(x) = \int_0^\infty \frac{\sin w^2}{w^2}\mathrm{e}^{-xw}\,\mathrm{d}w = (2\pi)^{1/2}\left\{\left[\frac{1}{2}-S\left(\frac{x}{(2\pi)^{1/2}}\right)\right]\cos\left(\frac{x^2}{4}\right)\right.$$
$$\left.-\left[\frac{1}{2}-C\left(\frac{x}{(2\pi)^{1/2}}\right)\right]\sin\left(\frac{x^2}{4}\right)\right\}-x\frac{\pi}{2}\left\{\left[\frac{1}{2}-C\left(\frac{x}{(2\pi)^{1/2}}\right)\right]^2+\left[\frac{1}{2}-S\left(\frac{x}{(2\pi)^{1/2}}\right)\right]^2\right\}.$$

Here, $S(x)$ and $C(x)$ are the Fresnel integrals (see Abramowitz & Stegun 1964). Although we have not been able to express $\mathscr{Y}(x)$ in terms of elementary functions, it is relatively easy to compute for small values of $x$. For large values of $x$, $\mathscr{Y}(x)$ can be approximated in terms of Fresnel integrals.

A similar calculation can be carried out for $x < -a$ where the only contribution comes from the pole $A(k_2)$. The result is

$$\hat{\eta}^0 \approx \frac{P_0}{\rho g}\left[\frac{4Q(A_0)}{\mathscr{D}_{k_1}(A_0,0)\,A_0}\sin\left(\frac{x}{H}A_0\right)\sin\left(\frac{a}{H}A_0\right)+\frac{2}{\pi}\frac{(a/H)(b/H)^{1/2}}{(\frac{1}{3}+\gamma)^{3/4}}\mathscr{W}\left(\frac{|x|/H}{(\frac{1}{3}+\gamma)^{1/4}(b/H)^{1/2}}\right)\right]. \quad \text{(B 9)}$$

Under the conditions where (B 8) and (B 9) are valid, it can be shown that the second integral in (B 5) is $O(1-F^2)^{1/2}$ for $F^2 < 1$ and $o(F^2-1)^{1/2}$ for $F^2 > 1$.

## REFERENCES


Abramowitz, M. & Stegun, I. A. 1964 *Handbook of Mathematical Functions*. National Bureau of Standards, Washington, DC.

Beltaos, S. 1981 Field studies on the responses of floating ice sheets to moving loads. *Can. J. Civ. Engng* **1**, 1–8.

Brochu, M. 1977 Air cushion vehicles. *Science Dimension* **9**, 16–19.

Cohen, H. & Clayton, A. 1982 Research into transport aspects of ice sheets. Office of Industrial Research, University of Manitoba.

Davys, J. W., Hosking, R. J. & Sneyd, A. D. 1985 Waves due to a steadily moving source on a floating ice plate. *J. Fluid Mech.* **158**, 269–287.

Eyre, D. 1977 The flexural motions of a floating ice sheet induced by moving vehicles. *J. Glaciol.* **19**, 555–570.

Greenhill, A. G. 1887 Wave motion in hydrodynamics. *Am. J. Maths* **9**, 62–112.

Hosking, R. J., Sneyd, A. D. & Waugh, D. W. 1988 Viscoelastic response of a floating ice plate to a steadily moving load. *J. Fluid Mech.* **196**, 409–430.

Isaacson, E. & Keller, H. B. 1966 *Analysis of Numerical Methods*. John Wiley & Sons.

Kerr, A. D. 1983 The critical velocities of a load moving on a floating ice plate that is subjected to in plane forces. *Cold Regions Sci. Tech.* **6**, 267–274.

Kheisin, D. Ye. 1963 Moving load on an elastic plate which floats on the surface of an ideal fluid (in Russian). *Izv. AN SSSR, Otd, Tekh. i Mashinostroenie* **1**, 178–180.

Kheisin, D. Ye. 1971 Some non-stationary problems of dynamics of the ice cover. In *Studies in Ice Physics and Ice Engineering* (ed. G. N. Iakolev). Israel Program for Scientific Translation.

LIGHTHILL, M. J. 1957 River waves. *Naval Hydrodynamics Publication* 515. National Academy of Sciences, National Research Council USA.

LIGHTHILL, M. J. 1978 *Waves in Fluids*. Cambridge University Press.

NEVEL, D. E. 1970 Moving loads on a floating ice sheet. *CRREL, Hanover, NH, USA*.

SCHULKES, R. M. S. M., HOSKING, R. J. & SNEYD, A. D. 1987 Waves due to a steadily moving source on a floating ice plate. Part 2. *J. Fluid Mech.* **180**, 297–318.

SCHULKES, R. M. S. M. & SNEYD, A. D. 1988 Time-dependent responses of floating ice to a steadily moving load. *J. Fluid Mech.* **186**, 25–46.

SZILARD, R. 1974 *Theory and Analysis of Plates*. Prentice-Hall.

TAKIZAWA, T. 1985 Deflection of a floating sea ice sheet induced by moving load. *Cold Regions Sci. Tech.* **11**, 171–180.

TAKIZAWA, T. 1988 Response of a floating sea ice sheet to a steadily moving load. *J. Geophys. Res.* **93** (C5), 5100–5111.

WHITHAM, G. B. 1974 *Linear and Nonlinear Waves*. John Wiley & Sons.